



Delft University of Technology

Dynamic stall on airfoils with leading-edge tubercles

Valls Badia, Pere; Hickel, Stefan; Scarano, Fulvio; Li, Mogeng

DOI

[10.1007/s00348-025-03981-7](https://doi.org/10.1007/s00348-025-03981-7)

Publication date

2025

Document Version

Final published version

Published in

Experiments in Fluids

Citation (APA)

Valls Badia, P., Hickel, S., Scarano, F., & Li, M. (2025). Dynamic stall on airfoils with leading-edge tubercles. *Experiments in Fluids*, 66(3), Article 56. <https://doi.org/10.1007/s00348-025-03981-7>

Important note

To cite this publication, please use the final published version (if applicable). Please check the document version above.

Copyright

Other than for strictly personal use, it is not permitted to download, forward or distribute the text or part of it, without the consent of the author(s) and/or copyright holder(s), unless the work is under an open content license such as Creative Commons.

Takedown policy

Please contact us and provide details if you believe this document breaches copyrights. We will remove access to the work immediately and investigate your claim.



Dynamic stall on airfoils with leading-edge tubercles

Pere Valls Badia¹ · Stefan Hickel¹ · Fulvio Scarano¹ · Mogeng Li¹

Received: 14 August 2024 / Revised: 20 January 2025 / Accepted: 24 January 2025
© The Author(s) 2025

Abstract

Leading-edge protuberances on airfoils have been shown to soften the onset of aerodynamic stall and to increase lift in the post-stall regime. The present study examines the effect of tubercles during dynamic stall. Pitching airfoils with tubercles of different amplitudes are studied by wind-tunnel experiments, where the three-dimensional time-resolved velocity field is determined using large-scale particle-tracking velocimetry. Computational fluid dynamics simulations are carried out that complement the experimental observations providing pressure distribution and aerodynamic forces. The dynamic stall is dominated by a vortex formed at the leading edge; we characterize the vorticity, circulation, and advection path of this dynamic-stall vortex (DSV). The presence of the tubercles profoundly modifies the boundary layer from the leading edge. The roll-up of the vorticity sheet is significantly delayed compared to a conventional airfoil, resulting in a weaker DSV. The vortex formation is shifted downstream, with the overall effect of a weaker and shorter lift overshoot, in turn enabling a quicker transition to deep stall. Regions of flow separation (stall cells) are visibly compartmentalized with a stable spacing of two tubercles wavelengths.

1 Introduction

Tubercles, a passive flow control device inspired by the unique protuberances along the leading edge of humpback whale (*Megaptera novaeangliae*) flippers, exemplify biomimicry in aerodynamics. Despite humpback whales reaching lengths up to 19 m and weights over 53 tons, they demonstrate exceptional agility, executing incredibly tight underwater maneuvers during their feeding routines. This remarkable maneuverability is attributed to the hydrodynamic advantages provided by the leading-edge tubercles which are not observed in other whale species (Fish and Battle 1995).

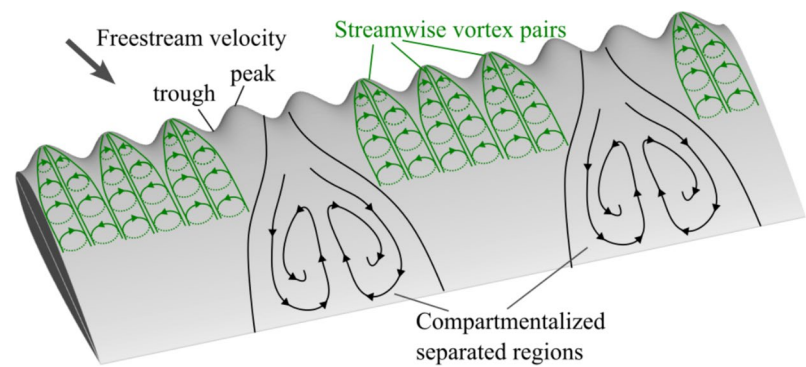
Motivated by these advantages, substantial research in aerodynamics has focused on understanding the flow mechanisms associated with the benefits of tubercles. Studies

considering airfoils in static conditions have shown that tubercles significantly alter aerodynamic performance: they soften the stall evolution, reduce the maximum lift, and enhance the post-stall performance compared to smooth leading-edge counterparts. These alterations are due to counter-rotating streamwise vortices (SV) generated by the tubercles, which enhance boundary layer mixing (Carreira Pedro and Kobayashi 2008; Hansen 2012) and compartmentalize flow separation regions into stall cells (Cai et al. 2017) as presented in Fig. 1. However, recent observations of humpback whales in their natural habitat have revealed rapid flipper movements during lunging maneuvers toward prey. The frequencies of these flapping motions fall within the realm of unsteady aerodynamics, as already pointed out by Hrynuk and Bohl (2020). They investigated the flipper motion of humpback whales observed during the feeding routine and estimated a non-dimensional pitch rate of $k = \dot{\alpha}c/2U \approx 0.2$, where $\dot{\alpha}$ is the pitching rate, c the airfoil (viz. flipper) chord and U is the flow velocity. Significant differences compared to the static stall characteristics are expected for this value. In fact, dynamic stall studies have shown that vortex formation and the associated vortex-induced peak lift can occur at frequencies as low as $k = 0.005$ (Choudhry et al. 2014). Combined with the incidence of the flipper being well above the static stall angle during the flapping stroke, this indicates the presence of a dynamic stall event. This insight indicates

✉ Mogeng Li
Mogeng.Li@tudelft.nl
Stefan Hickel
S.Hickel@tudelft.nl
Fulvio Scarano
F.Scarano@tudelft.nl

¹ Faculty of Aerospace Engineering, Delft University of Technology, Kluyverweg 1, 2629 HS Delft, South Holland, The Netherlands

Fig. 1 Airfoil geometry with leading-edge tubercles and schematic representation of streamwise vortices and compartmentalization effects



the need to study the effect of tubercles under dynamic conditions, as done in the recent work of Hrynyuk and Bohl (2020).

Dynamic stall is an unsteady flow phenomenon that occurs when an airfoil or wing rapidly pitches or plunges, and by doing so, it undergoes a rapid change in its apparent angle of attack. Under such circumstances, leading-edge separation is associated with the formation of a well-defined vortex, known as the dynamic stall vortex (DSV) (Visbal 1990). The latter, intensifies the suction effect above the leading edge and increases the maximum lift for a transient period, after which it is released from the airfoil, causing the stall. It has been reported that during dynamic stall the maximum lift can increase threefold compared to the static conditions (Choudhry et al. 2014).

Extensive studies on horizontal axis wind turbines (HAWTs) show that dynamic stall can be triggered by abrupt changes in inflow velocity, yaw operation, blade passage through the tower shadow, turbulence, and wind shear (Choudhry et al. 2013). Vertical axis wind turbines (VAWTs) are particularly prone to dynamic stall when operating at low tip-speed ratios ($\lambda < 3$) (Buchner et al. 2018). Similarly, dynamic stall frequently occurs across helicopter rotor blades during high-speed and maneuvering flights. The associated dynamic loads can result in excessive stresses and systems vibration and fatigue which reduce their operational lifespan (Butterfield et al. 1991). With this perspective, advances have been made in understanding the dynamic stall process with the aim of mitigating its detrimental effects (McCroskey 1981; Ferreira et al. 2009). Considering this scenario, gaining a deeper understanding of how tubercles influence the development of dynamic stall on airfoils could lead to significant engineering applications aimed at mitigating the severity of dynamic stall effects.

While the dynamic stall process on conventional airfoils, i.e., those with a straight leading edge, is well understood, the effect of tubercles on dynamic stall is only partially understood. The majority of the literature on dynamic stall with tubercled airfoils relies on the measurement of the aerodynamic forces to evaluate the impact of the tubercles (Borg

2012; Nayman and Perez 2022). For airfoils oscillating up to a maximum angle of attack below the static stall angle, tubercles mitigate hysteresis and reduce lift overshoot (Borg 2012; Cai et al. 2013). However, when the oscillation amplitude exceeds the static stall angle, some discrepancies are found in the research regarding the effect of tubercles on lift hysteresis or the lift overshoot. Therefore, the role of tubercles as either lift enhancement or dynamic stall mitigation devices remains uncertain.

The research conducted by Hrynyuk and Bohl (2020) stands out for the comprehensive analysis of the flow field, including a meticulous investigation of the DSV. Contrary to previous research, they report that for the tubercled airfoil, the DSV is stronger (i.e., has more intense circulation) and closer to the suction side of the airfoil. Furthermore, the above authors report that the DSV is advected at a lower speed compared to the conventional airfoil. Although aerodynamic forces were not directly measured during the experiments, the authors hypothesize that the combination of these factors increases the dynamic lift over an extended period compared to a traditional straight leading-edge airfoil. This suggests that tubercles might act as lift enhancement devices.

Other observations are somewhat contrasting with the above, with the hypothesis that tubercles essentially act to mitigate dynamic stall, rather than enhancing lift (Wu and Liu 2021; Nayman and Perez 2022). The flow mechanisms of tubercles under static conditions have been well-documented, but extending this knowledge to dynamic conditions requires the full understanding of the interplay between the leading-edge (streamwise) vortices and the formation and growth of the larger DSV with spanwise orientation. Studying the latter phenomenon proves challenging for experimental techniques, being intrinsically unsteady and three-dimensional (3D). In their recent study, Hrynyuk and Bohl (2020) provide a detailed flow field analysis for an airfoil with tubercles, with measurements covering two planes, one aligned with a trough and another with a peak, to describe the spanwise variation of the in-plane flow. The work extends previous studies based upon single-plane

measurements with particle-image velocimetry (PIV). However, some relevant flow properties, such as the spanwise velocity component and the streamwise vorticity distribution cannot be captured even with two separate planes.

The current study approaches the problem with the measurement of the time-resolved three-dimensional velocity and vorticity field, based on particle tracking. Although the technique offers a limited spatial resolution compared to planar PIV, it enables the simultaneous visualization of the instantaneous 3D velocity field and the velocity gradient tensor. The latter is pivotal to the analysis of vorticity and circulation, at the basis of leading-edge vortices and their interaction with the DSV. The work is corroborated with unsteady computational fluid dynamics (CFD) simulations matching the experimental conditions (airfoil motion and Reynolds number), which offer complementary information on quantities not available from the experiments, namely the pressure field and the associated aerodynamic force.

2 Methodology

2.1 Experimental setup

Experiments are conducted in the W-Tunnel (low-speed, open-return, closed test section) at the Aerodynamics Laboratory of TU Delft. The test section has a cross-sectional area of $0.6 \times 0.6 \text{ m}^2$ and a length of 1.2 m. The wind tunnel is operated at a free-stream velocity of $U_\infty = 5 \text{ m/s}$, corresponding to a Reynolds number of $Re = U_\infty c / \nu = 3.3 \times 10^4$ where ν is the kinematic viscosity of the air and c the mean airfoil chord length of $c = 0.1 \text{ m}$.

Although the Reynolds number in these experiments is lower than that of humpback whale flippers, where $Re \approx 2.5 \times 10^6$ based on chord length of $c = 0.82 \text{ m}$ and swimming velocity of 3 m/s (Hrynyuk and Bohl 2020), studies have demonstrated that the dynamic stall process and associated vortex structures are relatively insensitive to Reynolds number effects. While lower Reynolds numbers tend to increase the size of flow structures (Zhang and Schlüter 2012), the overall evolution of the DSV remains constant. Therefore, the findings and conclusions of this research can be reasonably extrapolated to higher Reynolds numbers encountered in real-world applications.

The symmetric NACA0021 airfoil is chosen as the baseline geometry for this study, as it closely resembles the cross section of the humpback whale flipper (Fish and Battle 1995). It is similar to NACA0020 and NACA0015 airfoils extensively used in prior studies (Miklosovic et al. 2007; Borg 2012).

The airfoil spans the full height of the test section ($b = 0.6 \text{ m}$), as shown in Fig. 2. Three geometries are considered: the first one has a straight leading edge, while the other two airfoil models feature tubercles with a chord-normalized amplitude A/c of 5% and 10%. Following previous studies, the tubercle wavelength λ is set to 25% of the chord ($\lambda/c = 0.25$). The resulting airfoils, with $A/c = [0, 0.05, 0.1]$ are denoted as the baseline, A05L25, and A10L25, respectively. Throughout this work, the straight leading-edge airfoil is referred to as the baseline. The three airfoil geometries are displayed in Fig. 3.

The airfoil motion follows a pitch-up rotation around the quarter-chord point, followed by a hold period as presented in Fig. 4. Such approach has been previously adopted in

Fig. 2 Schematic of the experimental setup in the W-Tunnel and PTV system layout

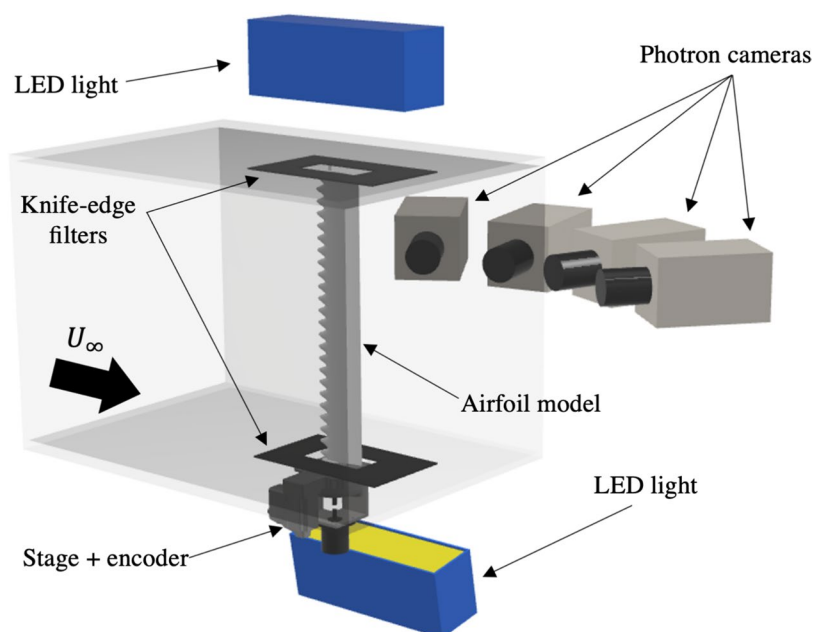


Fig. 3 Geometry of the baseline and tubercled airfoils

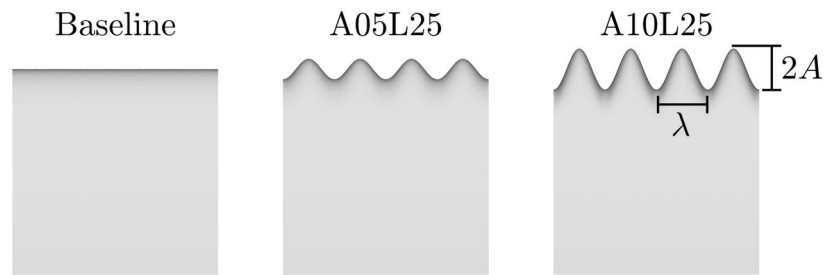
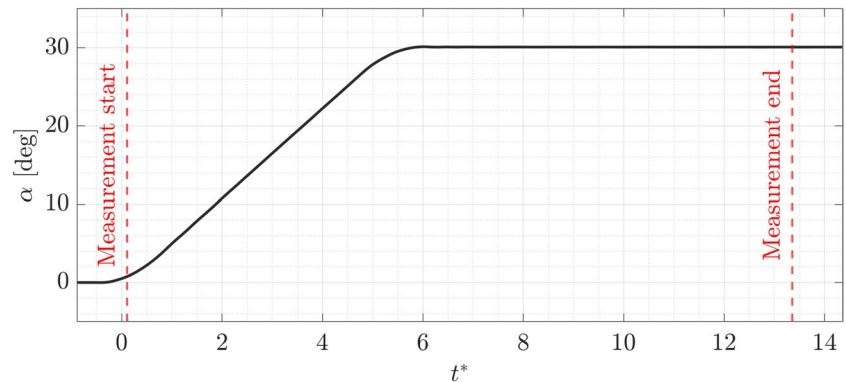


Fig. 4 Airfoil motion during the measurement phase



research related to dynamic stall of airfoils, with and without tubercles (Jumper et al. 1987; Gendrich 1999; Hrynyuk and Bohl 2020). Specifically, the airfoil is subject to pitch-up at a constant pitching rate $\dot{\alpha} = 5$ rad/s and hold at a maximum angle of attack $\alpha_{max} = 30^\circ$, well above the static stall angle of attack, which is found to be below 15° at this Reynolds number (Li and Scarano 2024). The pitching rate is expressed in non-dimensional form as $k = \dot{\alpha}c/2U_\infty = 0.05$.

The time is normalized ($t^* = tU_\infty/c$) and referred to a time origin where $t^* = 0$ is defined as the moment the airfoil reaches $\alpha = 0.5^\circ$. The airfoil remains at the maximum angle of attack until the measurement is complete. Afterward, the airfoil is brought back to zero incidence and held at a fixed position, allowing the flow field to stabilize before the start of the next cycle. The upstroke and downstroke pauses last for approximately 20 convective times ($t_{upstroke} = 20c/U_\infty$).

The airfoil motion is controlled by a rotary stage (X-RSB120AB-E08, Zaber Technologies Inc) installed at the lower wall of the wind tunnel (see Fig. 2). The airfoil position during the pitching motion is monitored with an Elap srl REV620 encoder.

2.2 Velocity measurements

The velocity field is measured on the suction side of the airfoil with 3D time-resolved particle tracking, following the setup and the wind-tunnel arrangement illustrated in Fig. 2. The flow is seeded with neutrally buoyant helium-filled soap bubbles (HFSB) with a nominal diameter of approximately $300 \mu\text{m}$ (Faleiros et al. 2019). These are introduced into the

settling chamber by a two-dimensional array comprising 200 generators (Huang et al. 2022). Air, soap, and helium flow rates are controlled by pressure regulation, with a fluid supply unit (FSU). At the given free stream velocity and with a rate of tracers generation (20000/s), the nominal seeding concentration can be estimated following (Caridi 2018) and it amounts to approximately 3 bubbles/cm^3 .

Illumination is provided by two LaVision *LED-Flashlight 300* sources positioned above and below the wind-tunnel section. Furthermore, to prevent illuminating particles that are too close or too far from the cameras, which may lie outside the depth of field, knife-edge filters are used to match the illuminated region to the measurement volume.

The 3D imaging system comprises four Photron Fastcam SA1.1 CMOS cameras (1 Mpx sensor, pixel pitch $20 \mu\text{m}$, 5400 fps). The cameras are placed at approximately 1 m distance from the airfoil and arranged in arc-like configuration, subtending a total angle of 40° . Nikon objectives with 60 mm focal length are used and set to a numerical aperture of $f_\# = 16$. The resulting magnification is $M = 0.066$ and focal depth $\delta_y = 0.17 \text{ m}$, yielding focused particle images over a measurement volume of $18 \times 12 \times 30 \text{ cm}^3$. Given the aspect ratio of the region of interest, the active sensor size was reduced to 768×1024 pixels.

The system is operated at 2000 frames/s, capturing the tracers motion around the airfoil for a duration of 3.6 s. Each acquisition comprised up to 4×7276 images, covering 10 full pitch and hold cycles. Image recording and illumination are synchronized with a LaVision programmable timing unit (PTU) and controlled through the DaVis software.

Table 1 Experimental parameters for PTV measurements

Field of view (3D domain)	$18 \times 12 \times 30 \text{ cm}^3$
Number of cameras	4
Observation distance	$\sim 1 \text{ m}$
Recording device	Photron Fastcam SA1.1 CMOS (1 Mpx sensor)
Recording lens	60 mm Nikon $f_{\#} = 16$
Illumination	LaVision LED-Flashlight 300×2
Recording frequency	2000 Hz (illumination pulse: 50 microseconds)
Seeding tracers	HFSB, $d = 300 \mu\text{m}$

Parameters of the PTV measurements are summarised in Table 1.

A LabView program is employed to synchronize the cameras with the motion of the airfoil, utilizing the encoder to record the angle of incidence at a sampling rate of 2000 Hz. The image acquisition is triggered by a signal sent to the PTU when the airfoil reaches $\alpha = 0.5^\circ$ during the pitch-up phase. This real-time triggering is enabled by the NI Compact RIO hardware, ensuring that all measurements commenced at the same phase of the pitch-up movement over all the cycles.

The particles motion analysis is performed with the DaVis 10 software, using the Shake-the-Box (STB) algorithm (Schanz et al. 2016) to process images. A representative image of the particles, as obtained during these research experiments, is displayed in Fig. 5a.

The reflections from the airfoil leading edge are eliminated by image pre-processing making use of a temporal high-pass filter (Sciacchitano and Scarano 2014). The resulting images feature an average particle image density $ppp = 0.03$, which corresponds to approximately 0.8 tracers/cm^3 . The latter is below the nominal value of the seeder, ascribed to some inoperative generators.

The Shake-the-Box algorithm yields approximately 1.5×10^4 tracks in the measurement volume at each time instant as illustrated by an example in Fig. 5b.

The scattered data are reduced to a Cartesian grid by a local average into cubic bins of 10.8 mm length. Neighboring bins overlap by 75% yielding a grid step of 2.7 mm ($0.027c$). In order to accumulate sufficient tracers data into each bin, a temporal average over 21 time-steps (10 ms, or $\Delta t^* = 0.52$) is considered. For the spatial as well as temporal average, the data are fitted with a first-order polynomial inside each bin, following (Discetti et al. 2015).

2.3 RANS simulations

Complementary to the experiments, CFD simulations are utilized to model the unsteady aerodynamic behavior with the specific purpose of capturing the aerodynamic forces not available from the experiments. The numerical simulations are conducted using the DelftBlue supercomputer (Delft High Performance Computing Centre (DHPC), 2024) and the open-source CFD software OpenFOAM. Specifically, the *pimpleFoam* solver, which is particularly suitable for incompressible, transient and turbulent flows, is utilized to solve the unsteady Reynolds-averaged Navier–Stokes (URANS) equations with the $k - \omega$ SST turbulence model.

Mesh generation is performed with *SnappyHexMesh*, to construct a hexahedral mesh around the airfoil. Four layers are employed to ensure that the viscous sub-layer of the boundary layer is well resolved. To facilitate the intended rotation of the airfoils, a sliding mesh approach is implemented, following the methodology of Zhao et al. (2021) and Rohmawati et al. (2020). The interface between the stationary outer domain and the rotating subdomain is a cylindrical surface surrounding the airfoil, see Fig. 6. The diameter of this cylinder is four times the airfoil chord, and it is centered at $x/c = 0.25$ to match the wind-tunnel model. The computational domain recreates the wind-tunnel conditions, with

Fig. 5 Left: particle image recording (raw image). Right: an instantaneous sample of particle tracks with 3 frames duration. The tracks are color-coded by streamwise velocity ($\alpha = 30^\circ$)

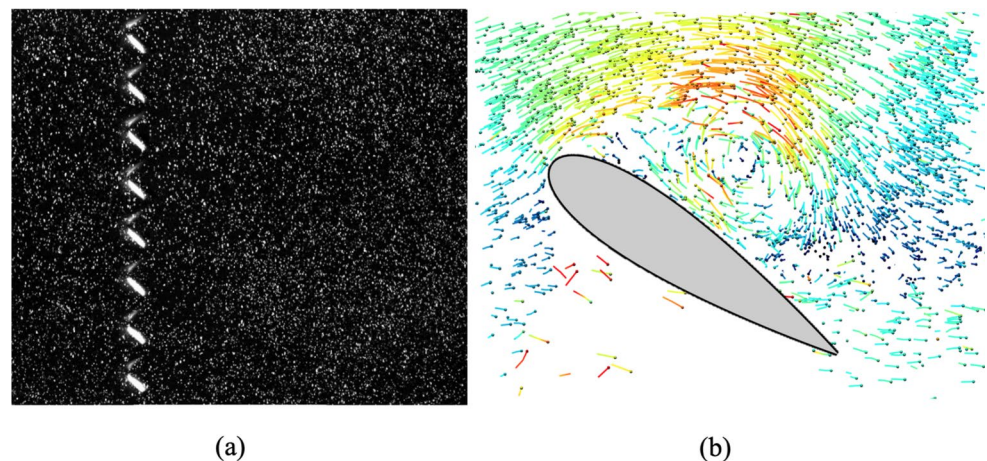
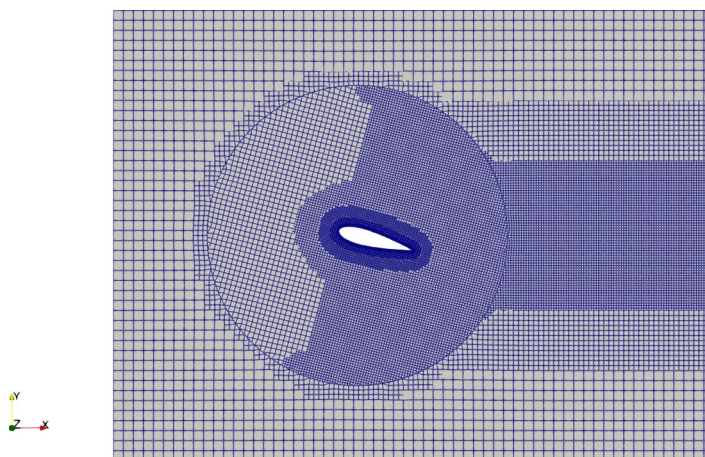


Fig. 6 CFD domain discretization with fixed (external) mesh and rotating (internal) mesh around the airfoil ($\alpha = 15^\circ$)



inlet and outlet boundaries placed at 3 chords upstream and 5 chords downstream, respectively. The resulting computational grid has approximately 17×10^6 elements.

No-slip boundary conditions are imposed for the airfoil surface, and slip boundaries are applied to top and bottom walls. Symmetric boundary conditions are set at the side walls (Visbal and Garmann 2018). The initial condition for the transient solver is the steady-state solution for $\alpha = 0^\circ$ obtained with the *simpleFoam* steady-state solver, which is iterated until the normalized residuals of the velocity, pressure, and turbulence fields converge below 10^{-5} . A time step of $\Delta t = 5 \times 10^{-4}$ s is selected for the unsteady simulations.

The two-equation $k - \omega$ SST turbulence model is chosen due to its proven ability to accurately capture flow separation phenomena (Menter et al. 2003). This turbulence modeling technique has been demonstrated to yield good agreement with experimental data for both static and pitching airfoils

across a broad range of Reynolds numbers (Cai et al. 2017; Wu and Liu 2021).

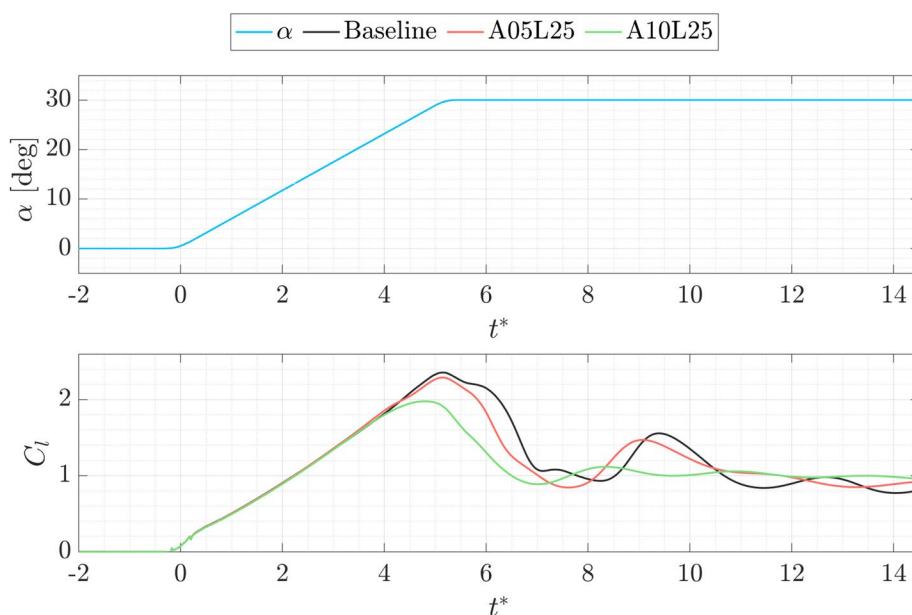
3 Results

3.1 Lift coefficient

For brevity, the following discussion of aerodynamic forces obtained from CFD focuses on the lift coefficient C_l only, which is presented in Fig. 7. This is justified by the prominent role of the dynamic stall vortex and the associated lift overshoot.

All considered cases exhibit the same linear range up to $t^* = 3.5$ ($\alpha = 20^\circ$). The slightly positive lift at the beginning of the cycle is due to the motion ramping up slightly before $t^* = 0$. Beyond $t^* = 4$, the smooth airfoil exhibits a further

Fig. 7 Top: airfoil motion (angle of attack time evolution) for reference. Bottom: lift coefficient time evolution (computed with CFD) for baseline, A05L25, and A10L25 airfoils undergoing pitch-up and hold motion with ($k = 0.05$)



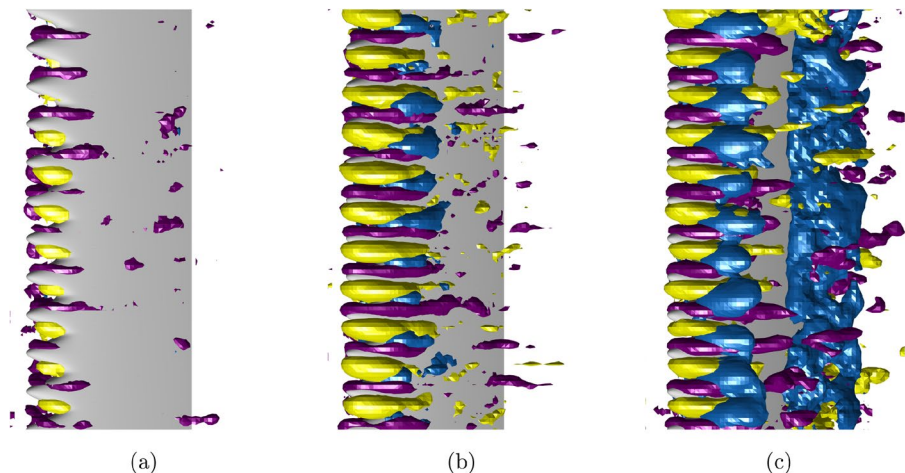
increase in lift, attaining a maximum $C_l = 2.3$ coinciding with the end of the pitching ramp. The A05L25 tubercled airfoil exhibit minimal departure from the baseline. Instead, the A10L25 tubercled airfoil reaches maximum lift ($C_l = 1.95$) at an earlier stage. Moreover, the tubercled airfoils enter more rapidly into the deep stall regime yielding a more stable (lower max-min) lift response overall.

The slightly different levels of lift during deep stall are considered negligible and only shortly mentioned here. This minimal variation is due to the airfoil being pitched well beyond the static stall angle of attack, where the reported stall mitigation effects of tubercles are not expected. At these high angles of attack, although the compartmentalization effect is visible with the tubercled airfoils, the attached regions between stall cells do not extend beyond the mid-chord position (Cai et al. 2017), thereby having a minimal effect on the total lift of the airfoil. Yasuda et al. (2019) also noted that the benefits of tubercles diminish around $\alpha = 30^\circ$. It is important to mention that the baseline airfoil exhibits a second lift peak before entering the deep stall regime. This peak is attributed to a second leading-edge vortex following the DSV convection, which is described in detail in Sect. 3.5.

3.2 Streamwise vorticity

Under static conditions, the most significant effect of leading-edge tubercles is the generation of a system of counter-rotating pairs of streamwise vortices (SV), as extensively documented in the literature (Custodio 2007; Carreira Pedro and Kobayashi 2008). Our data indicate that this phenomenon is also observable under dynamic conditions and persists throughout the entire pitch-up motion. Consistent with previous research conducted in static conditions, the vortex pair induces downwash along the tubercle peaks and upwash at the troughs.

Fig. 8 Streamwise and spanwise vorticity field evolution during the pitching motion of the A10L25 airfoil at **a** $\alpha = 10^\circ$, $t^* = 1.9$; **b** $\alpha = 20^\circ$, $t^* = 3.6$; **c** $\alpha = 30^\circ$, $t^* = 6$. Iso-surfaces at $\omega_x c/U_\infty = -1.5$ (yellow), 1.5 (purple) and $\omega_z c/U_\infty = -7$ (blue)



This downwash-upwash strongly modulates the shear layer of the developing boundary layer, which in turn plays a role in the formation and growth of the DSV as detailed further in Sect. 3.3. Note that the vorticity and velocity fields presented in Sects. 3.2 and 3.3 are from the experiments. Figure 8 illustrates the streamwise vortices emanating from the tubercled leading edge, by means of normalized streamwise vorticity, during airfoil pitching. An animation of the flow field (and subsequent flow field figures) is included in the Supplementary Materials. At 10 degrees ($t^* = 2$), such vortices develop till approximately one-quarter chord. Increasing pitch, they are observed to propagate further along the airfoil surface till half chord. Although their intensity has increased compared to the previous condition, they appear to stop abruptly, which suggests an intense activity of vorticity tilting, presumably in the spanwise direction, or negative stretching, due to local flow separation and deceleration. This occurs as the DSV begins to develop at this chord location, gaining strength (spanwise vorticity). Clearly, the two vortex systems cannot coexist and the DSV growth is performed at the expenses of the SV. The SV are tilting and breaking down to partially merge into the large spanwise vortical structure of the DSV.

3.3 DSV formation and growth

The spanwise vorticity distribution is illustrated and compared between the smooth leading edge and the A10L25 airfoils in Figs. 9 and 10, respectively. Given the higher intensity of the DSV, compared to the SV, vorticity iso-surfaces at $\omega_z c/U_\infty = -7$ are selected. The dynamical evolution of the DSV occurs at a later stage of the pitching motion and is represented at $t^* = [5, 6, 7]$ ($\alpha = [28^\circ, 30^\circ, 30^\circ]$), covering the phase of lift overshoot (refer to $C_l(t^*)$ from Fig. 7). In line with previous research on dynamic stall (Carr et al. 1977; Jumper et al. 1987; Gendrich 1999), both the baseline and the tubercled airfoils exhibit the dynamic stall phenomenon,

featuring flow separation at the suction side and the formation of the DSV as the airfoil deepens the pitching motion.

For the baseline airfoil, we observe that as soon as the flow separates and a recirculation region is formed in the fore part of the airfoil (Fig. 9), the vorticity sheet of the separated shear layer is re-ingested in the spanwise vortex from the reattachment line, leading to the growth of the DSV. The process is not sustained after the end of the pitching motion, when the vorticity supply is interrupted by the small, secondary recirculation formed ahead of the DSV, with consequent vortex detachment and advection downstream.

The presence of tubercles (Fig. 10) significantly alters the above scenario: we observe a strong spanwise modulation of the shear layer (i.e., the sheet of spanwise vorticity), which forms at the tubercles' troughs and maintains the boundary layer attached. A noticeably weaker DSV appears at a more downstream location (Fig. 10b), with the vorticity sheet already interrupted. At the end of the pitching motion (Fig. 10c), the weak vorticity filament above the airfoil aft part suggests that the vortex has commenced advection

earlier, in agreement with the time diagram of lift coefficient shown in Fig. 7. In summary, effects of the tubercles on the DSV are twofold: first, the counter-rotating streamwise vortices generated by the tubercles significantly inhibit vorticity ingestion into the DSV, reducing its strength and spanwise coherence; second, the presence of tubercles also contributes to an earlier detachment of the DSV.

A planar visualization of the flow field during DSV formation and development is shown on 2D slices in Fig. 11, following the approach proposed by Hrynuk and Bohl (2020). At $t^* = 5$, which corresponds to the condition of maximum lift, the shear layer emanating from the leading edge is visible, with the inception of a thin separation bubble at approximately $x/c = 0.15$ (Fig. 11a). The latter initiates the process of vorticity roll-up and DSV growth.

Two secondary, counter-rotating structures are formed (Fig. 11b), the first at the trailing edge of the airfoil, as a result of flow separation from the sharp edge. The second counter-rotating vortex is located just behind the separation line, as a result of the adverse pressure gradient experienced

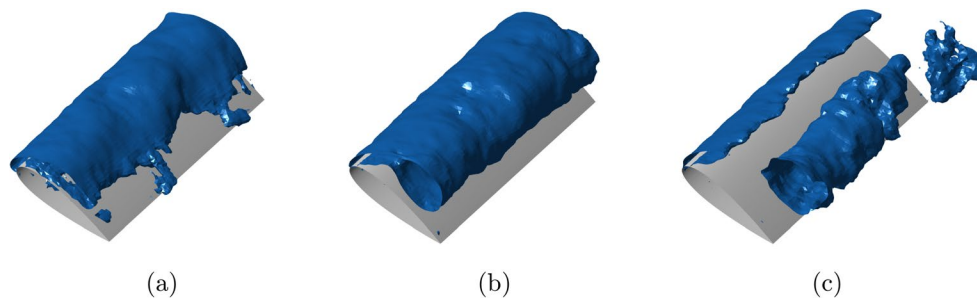


Fig. 9 Spanwise vorticity at **a** $\alpha = 27.9^\circ$, $t^* = 5$; **b** $\alpha = 30^\circ$, $t^* = 6$; **c** $\alpha = 30^\circ$, $t^* = 7$; for the baseline airfoil. Iso-surface at $\omega_z c/U_\infty = -7$

Fig. 10 Spanwise vorticity at **a** $\alpha = 27.9^\circ$, $t^* = 5$; **b** $\alpha = 30^\circ$, $t^* = 6$; **c** $\alpha = 30^\circ$, $t^* = 7$; for the A10L25 airfoil. Iso-surface at $\omega_z c/U_\infty = -7$

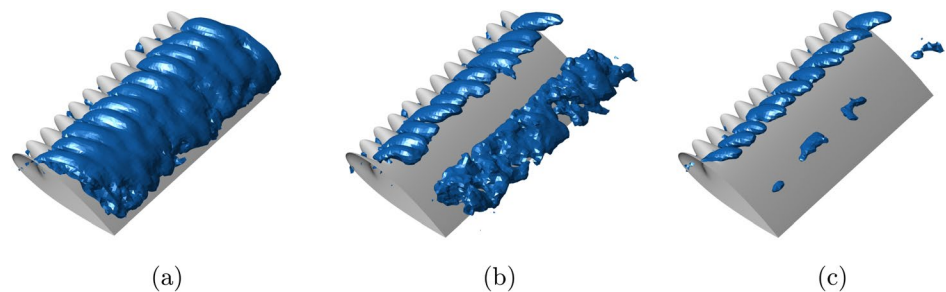
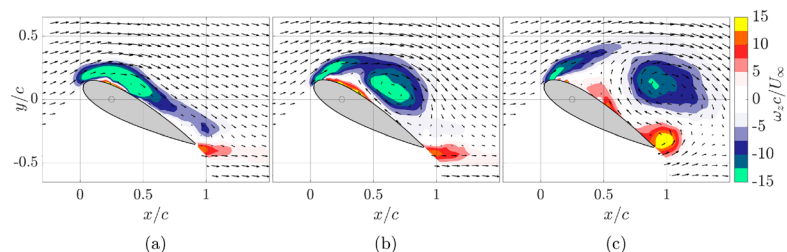


Fig. 11 Dynamic evolution of velocity and spanwise vorticity at the end of the pitching motion during the DSV formation and detachment stages for the baseline airfoil. From left to right: **a** $\alpha = 27.9^\circ$, $t^* = 5$; **b** $\alpha = 30^\circ$, $t^* = 6$; **c** $\alpha = 30^\circ$, $t^* = 7$



by the reverse flow induced below the DSV. In combination with the DSV, while growing, this structure is responsible for interrupting the process of vorticity feed from the separated shear layer into the DSV. As suggested by Hrynyuk and Bohl (2020), this secondary vorticity structure also causes the DSV to move upward and eventually detach. The limited spatial resolution leads to some underestimation of the intensity for this vorticity structure near the airfoil surface. Insufficient particle seeding in certain regions necessitates the use of spatial and temporal binning to improve data quality. However, this method requires larger spatial bins, which smooth out sharp velocity gradients and introduce temporal smearing, leading to a reduced accuracy in resolving near-wall vorticity. Nevertheless, the local flow topology suggests its presence and it has been clearly identified also in the CFD results. At a later stage, the DSV increases in size and strength and after $t^* = 6$, it is released as a distinct vortical structure (see Fig. 11c). However, as it moves away from the airfoil surface its influence on the airfoil lift is expected to decline, and the deep stall conditions are initiated (refer to Fig. 7). Finally, the DSV convects downstream. Its development under the effect of turbulent diffusion and its own instabilities eventually leads to breakdown, but the latter stages are not captured within the limits of the measurement domain. This pattern of DSV evolution aligns with previous studies on dynamic stall in smooth leading-edge airfoils (Jumper et al. 1987; Gendrich 1999).

The evolution of the velocity and vorticity field for the tubercled airfoil A10L25 is shown at two spanwise cross sections, the tubercle peak and tubercle trough, in Figs. 12 and 13, respectively. At the plane aligned with the tubercle peak, the flow exhibits a later separation but more pronounced than for the baseline at $t^* = 5$. This difference is ascribed to the streamwise vortex pair producing a downwash along the peak plane, which significantly delays separation. As

the angle of attack increases, ($t^* = 6$), the DSV in becomes more clearly visible, but with noticeably lower levels of vorticity compared and at a location closer to the airfoil surface and more downstream. This suggests that tubercles do not delay the temporal onset of the DSV, instead they relocate its formation downstream, reducing its influence on the lift overshoot.

On the trough plane (Fig. 13), flow separation appears to originate at the (local) leading edge of the airfoil. The evolution from the initial stage of the pitching motion ($t^* = 5$, Fig. 13a) features a separated shear layer with higher inclination upward, compared to the airfoil surface. The boundary layer vorticity is concentrated at the leading edge and the shear layer is strongly curved, encapsulating a small region of almost stagnant reverse flow. In this case the upwash induced by the SV prompts immediate local separation. This phenomenon, previously identified in the experiments of Hrynyuk and Bohl (2020), is likely to prevent the DSV from forming near the leading edge as a coherent vortical structure. By $t^* = 6$, the DSV position corresponds to that in the peak plane, indicating that the DSV motion dominates over the spanwise modulation of the SV. Approximately at $t^* = 7$, the DSV has already broken down under the action of the forcing SV. This observation corresponds to the CFD results, which indicate that the tubercled airfoil enters a deep stall regime more rapidly than the smooth leading-edge airfoil.

In all three planes, the pressure-side flow rolls up over the trailing edge, creating a vortex counter-rotating with respect to the DSV. The tubercled airfoil scenario, characterized by a weaker DSV, results in reduced downwash on the trailing edge, thereby facilitating the formation of a stronger trailing-edge vortex. Note that this trailing-edge vortex has minimal impact on the airfoil's total lift, as evidenced by the CFD results presented in Sect. 3.1.

Fig. 12 A10L25 airfoil spanwise vorticity field at tubercle peak position. From left to right: **a** $\alpha = 27.9^\circ$, $t^* = 5$; **b** $\alpha = 30^\circ$, $t^* = 6$; **c** $\alpha = 30^\circ$, $t^* = 7$

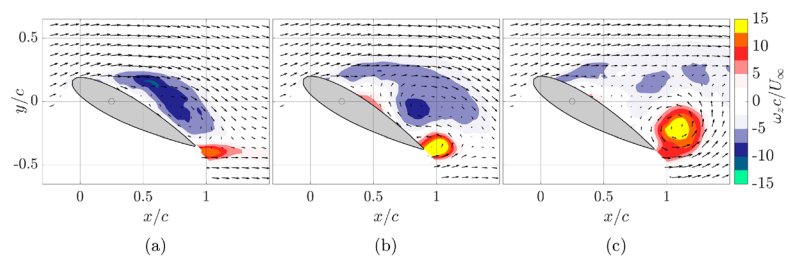
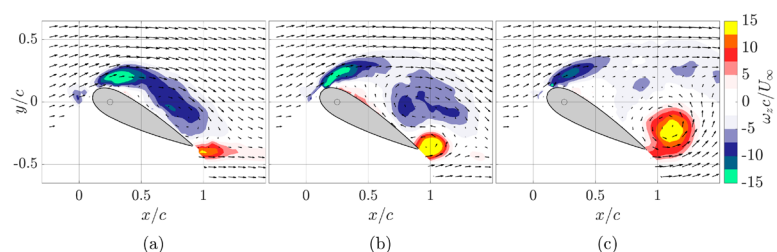


Fig. 13 A10L25 airfoil spanwise vorticity field at tubercle trough position. From left to right: **a** $\alpha = 27.9^\circ$, $t^* = 5$; **b** $\alpha = 30^\circ$, $t^* = 6$; **c** $\alpha = 30^\circ$, $t^* = 7$



3.4 DSV advection path and circulation

The advective path and strength of the DSV significantly impact the lift and drag characteristics of the airfoil (Carr et al. 1977; Jumper et al. 1987). The temporal evolution of the DSV and its interaction with tubercles has been qualitatively characterized in Sect. 3.3. In this section, the Γ_1 method (Michard et al. 1997) is used to perform temporal and spatial tracking of the DSV during airfoil pitch-up motion and to provide further quantitative information regarding the DSV evolution. This vortex identification method has been successfully applied to track the DSV captured with PIV (Taylor and Amitay 2016) and molecular tagging velocimetry (MTV) (Hrynuik and Bohl 2020). Moreover, once the core of the DSV is located in space, its circulation can be determined. To ensure comparability with the findings of Hrynuik and Bohl (2020), the circulation has been computed using the same methodology. In this section, the airfoil coordinate system is utilized, with the x_{AF} axis aligned with the chord direction and the origin set at the leading edge of the baseline airfoil. The y_{AF} axis is perpendicular to the x_{AF} axis and points outward from the airfoil's suction side. This specific frame of reference is particularly well-suited for pinpointing the position of the dynamic stall vortex (DSV) in relation to the airfoil rather than within the broader measurement volume, thus allowing for the study of relational effects between the DSV and the airfoil.

The convective path and circulation of the DSV for the three airfoils have been determined using experimental and CFD results. For effective tracking, the presence of a clear reverse-flow region is necessary. Prior to $t^* = 5$, where the airfoil approaches its maximum angle of attack of $\alpha_{max} = 30^\circ$, the Γ_1 method could not effectively determine the position of the DSV core, as it had not yet developed a well-defined structure for any of the airfoils. Similarly, the breakdown of the DSV, coupled with interference from the TE vortex, disrupts the rotational flow field, complicating accurate detection by the algorithm, which accounts for the varying tracking end times for each airfoil. It is important to note that since the pitch-up motion of the airfoil concludes by $t^* = 5$, any subsequent movement of the DSV can be attributed solely to its advection, rather than to a relative displacement between the DSV and the airfoil caused by the pitching motion.

Overall, both experimental and CFD results are in good agreement for the DSV path and circulation, see Fig. 14. For the DSV position, the simulations predict a slightly larger distance from the airfoil center-line y_{AF} than the wind-tunnel measurements. A notable difference lies in the circulation of the DSV during its early formation stages ($t^* < 6$), where CFD indicates higher circulation levels for all three airfoils. This can be attributed to the higher spatial resolution of the CFD simulations. Despite these discrepancies, CFD and experimental

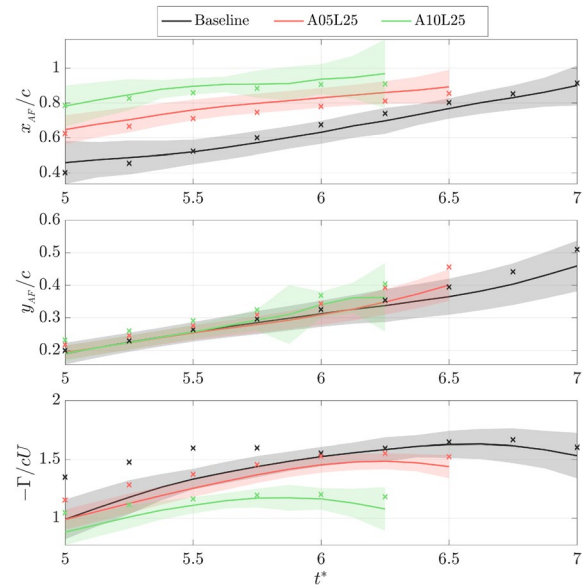


Fig. 14 DSV advection path and circulation for baseline and tubercled airfoils undergoing pitch-up and hold motion with $k = 0.05$ and $\alpha_{max} = 30^\circ$. The solid lines depict the spanwise average of the DSV core position obtained from experimental measurements, incorporating data from ten repetitions of each cycle. The shaded area represents the range within one standard deviation from the average. The CFD results are indicated by the \times markers

results align well, leading to consistent conclusions in line with the flow field observations. Firstly, the DSV forms closest to the leading edge at approximately $x_{AF}/c \approx 0.4$ for the baseline airfoil, while for the A05L25 and A10L25 airfoils, it forms further downstream at $x_{AF}/c \approx 0.6$ and $x_{AF}/c \approx 0.8$, respectively. Secondly, the presence of tubercles reduces the circulation of the DSV throughout the entire advection phase, with the largest tubercle amplitude resulting in the weakest DSV.

These observations indicate that tubercles not only shift the DSV formation further downstream, affecting a smaller portion of the airfoil chord, but also reduce the circulation of the DSV. This leads to a reduction in both the strength and duration of the lift overshoot, as identified from both experimental flow field analysis and the CFD aerodynamic forces. Moreover, larger tubercle amplitudes have a more pronounced impact on the dynamic stall phenomena. This suggests that tubercles effectively act as dynamic stall mitigation devices, reducing the intensity and duration of lift overshoots, thereby enhancing overall aerodynamic stability during dynamic stall conditions. This can be especially beneficial for airfoils operating in a wide range of conditions, such as wind turbine blades and helicopter rotors, which regularly experience dynamic stall.

In these applications, minimizing lift hysteresis and reducing cyclic structural loads can significantly improve performance and durability.

3.5 Deep stall regime

During the formation and growth of the DSV, flow reversal between the airfoil and the DSV is already visible. For the baseline airfoil, the reverse-flow patches are randomly distributed across the entire airfoil span, as shown in Fig. 15a. In contrast, for the tubercled airfoil, flow reversal regions become evident at nearly each trough, as depicted in Fig. 16a. This phenomenon is driven by the counter-rotating vortices shed by the tubercles. As the DSV is advected downstream and moves away from the airfoil surface, the separation region expands away from the airfoil surface, covering almost the entire airfoil span for the baseline scenario (see Fig. 15b). For the tubercled airfoil, the compartmentalization of the reverse-flow region becomes evident in Fig. 16b. The stall begins to reorganize into fewer but larger and more defined stall cells around approximately $t^* = 6.5$ as shown in Fig. 16c.

After the maximum lift is achieved, the influence of the DSV on the airfoil diminishes promptly, marking a transition to deep stall conditions characterized by a rapid decline in dynamic lift and a subsequent stabilization of the aerodynamic loads as the flow field evolves into a steady state. In the scenario of the pitch-up and hold motion employed in this research, with a reduced frequency of $k = 0.05$ and an initial pitch angle of $\alpha_{max} = 30^\circ$, the lift overshoot concludes approximately at $t^* = 6.75$ for the A10L25 airfoil and $t^* = 8$

for the baseline airfoil, indicating a more rapid transition of the tubercled airfoil into deep stall conditions.

As evidenced by the lift evolution predicted with CFD (see Fig. 7), a second smaller lift peak is observed immediately following the lift overshoot, before the lift stabilizes. This phenomenon is elucidated by Figs. 17 and 18, where the wake detachment process for the baseline and tubercled airfoils is illustrated. A 2D slice of the wake flow field evolution is also shown in Fig. 19 for the baseline case, to exemplify the role of free-stream flow in the wake detachment process. In both scenarios, although detachment occurs at different times, the flow evolution follows a similar pattern: the wake detachment begins when the trailing-edge vortex downwashes over the rear portion of the airfoil (panel a in Figs. 17, 18 and 19), pushing the reverse-flow region upstream, closer to the leading edge. Subsequently, the ascending trailing-edge vortex lifts the wake upward (panel b). Eventually, the vortex rises sufficiently to allow some of the free-stream flow to pass beneath it, effectively splitting the wake and triggering the formation of a second leading-edge vortex (panel c). This new vortex, similar to the DSV but with reduced strength, results in the second lift peak. After detachment, the trailing-edge vortex moves too far downstream from the airfoil to influence the separated flow, and the wake stabilizes.

The wake oscillations suggest that the airfoils transition into a vortex shedding mode before reaching deep stall conditions and lift levels stabilize. This peak is more pronounced in the baseline case, though it is still discernible with the tubercled airfoil. The vortex shedding is depicted in Fig. 20 for the baseline airfoil and in Fig. 21 for the tubercled

Fig. 15 Baseline airfoil stall cells formation during pitch-up motion at **a** $\alpha = 26.5^\circ$, $t^* = 4.75$; **b** $\alpha = 30^\circ$, $t^* = 5.75$; **c** $\alpha = 30^\circ$, $t^* = 6.5$. Iso-surface of stream-wise velocity $U_x/U_\infty = -2 \times 10^{-3}$

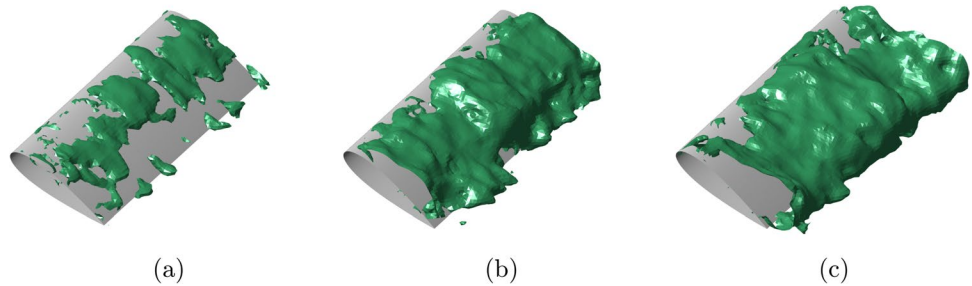


Fig. 16 A10L25 airfoil stall cells formation during pitch-up motion at **a** $\alpha = 26.5^\circ$, $t^* = 4.75$; **b** $\alpha = 30^\circ$, $t^* = 5.75$; **c** $\alpha = 30^\circ$, $t^* = 6.5$. Iso-surface of stream-wise velocity $U_x/U_\infty = -2 \times 10^{-3}$

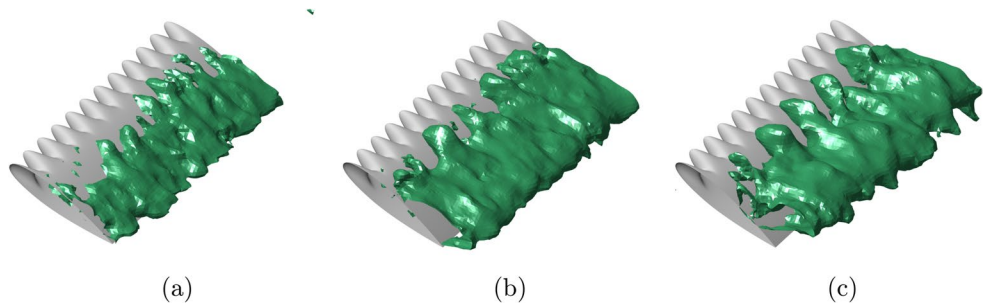


Fig. 17 Wake detachment event, captured for the baseline airfoil at **a** $\alpha = 30^\circ$, $t^* = 8$; **b** $\alpha = 30^\circ$, $t^* = 9.25$; **c** $\alpha = 30^\circ$, $t^* = 11.2$. Iso-surface of streamwise velocity $U_x/U_\infty = -2 \times 10^{-3}$

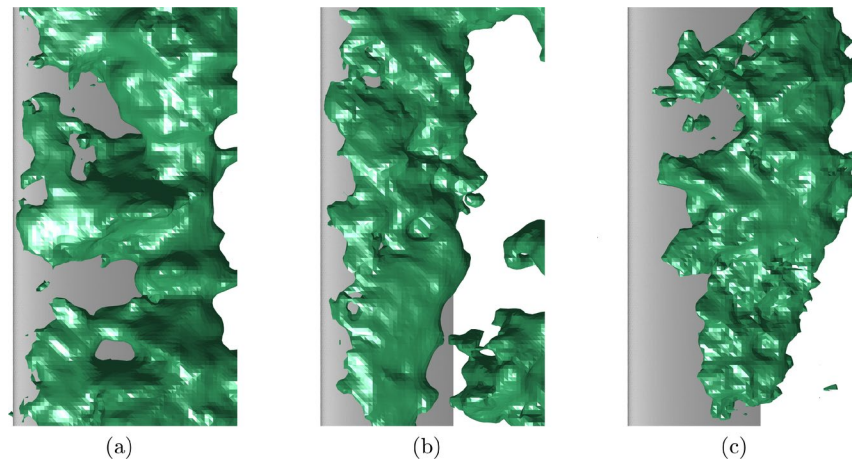


Fig. 18 Wake detachment event, captured for the tubercled airfoil A10L25 at **a** $\alpha = 30^\circ$, $t^* = 6.75$; **b** $\alpha = 30^\circ$, $t^* = 8$; **c** $\alpha = 30^\circ$, $t^* = 9.5$. Iso-surface of streamwise velocity $U_x/U_\infty = -2 \times 10^{-3}$

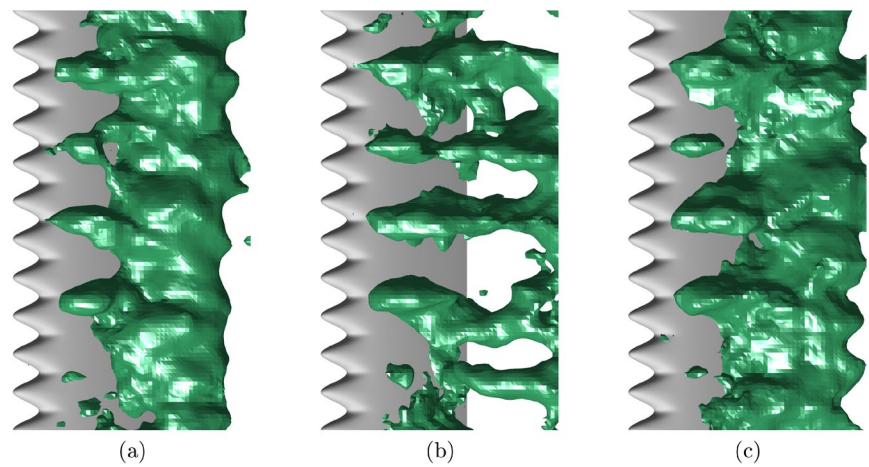


Fig. 19 Instantaneous velocity vectors and streamwise velocity contours for the baseline airfoil during wake detachment at **a** $\alpha = 30^\circ$, $t^* = 7$; **b** $\alpha = 30^\circ$, $t^* = 8$; **c** $\alpha = 30^\circ$, $t^* = 9.25$

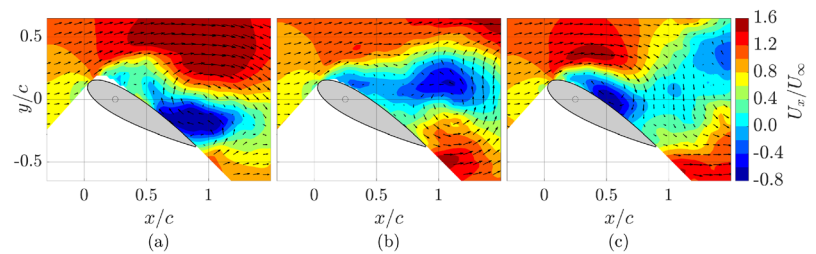
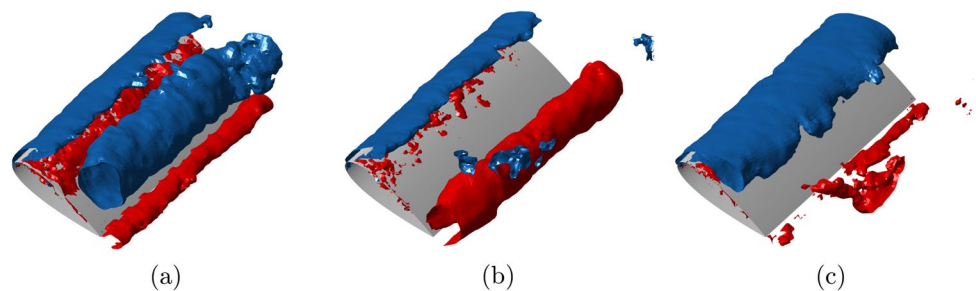


Fig. 20 Baseline airfoil vortex shedding evolution at **a** $\alpha = 30^\circ$, $t^* = 6.5$; **b** $\alpha = 30^\circ$, $t^* = 8$; **c** $\alpha = 30^\circ$, $t^* = 9.25$. Iso-surfaces at $\omega_z c/U_\infty = -7$ (blue) and 7 (red) showing the leading and trailing-edge vortices



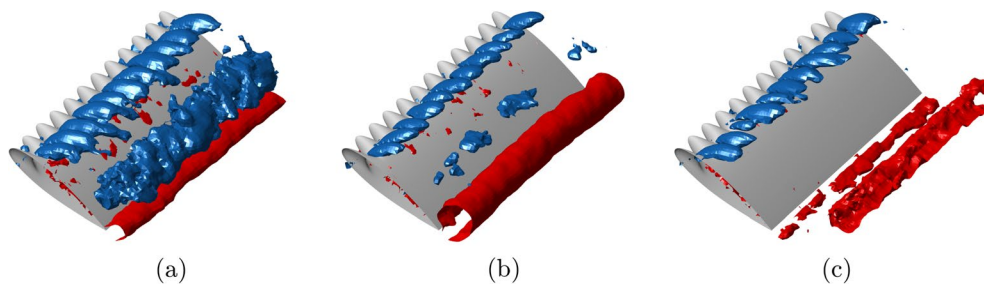


Fig. 21 A10L25 airfoil vortex shedding evolution at **a** $\alpha = 30^\circ$, $t^* = 5.75$; **b** $\alpha = 30^\circ$, $t^* = 6.75$; **c** $\alpha = 30^\circ$, $t^* = 8$. Iso-surfaces at $\omega_z c/U_\infty = -7$ (blue) and 7 (red) showing the leading and trailing-edge vortices

case. For the baseline, it is clearly visible that a second spanwise vortex is shed from the leading edge after the trailing-edge vortex detaches. Notably, at $t^* = 9.25$, the wake is effectively split, and the leading-edge vortex approaches the quarter-chord position. This time instant coincides with the moment when the CFD-predicted forces indicate the second lift peak for the baseline. Conversely, for the A10L25 airfoil, the DSV forms further downstream, leading to its earlier advection past the trailing edge compared to the baseline case. Consequently, the trailing-edge vortex rolls up more rapidly, and the wake detachment occurs sooner. The resulting second leading-edge vortex is substantially weaker and is not visible in Fig. 21, explaining the minimal secondary lift peak observed for the tubercled airfoil in the simulations.

Following the shedding of the second leading-edge vortex, the wake stabilizes and the strength of the vortex shedding is drastically reduced, consistent with the lift levels predicted by CFD, which show minimal oscillations. In this regime, which is shown in Fig. 18c, the airfoils exhibit behavior similar to previous experiments conducted under static conditions (Custodio 2007; Cai et al. 2017), where the effect of compartmentalization is observed with stable stall cells along the airfoil span. Interestingly, while the stall cells maintain consistent positions throughout each motion cycle, their positioning exhibits random variations across different cycles. It has also been observed that the spacing between consecutive stall cells λ^* varies, ranging from one to three wavelengths, with a predominant configuration of $\lambda^*/\lambda = 2$ in line with previous experiments in static conditions (Rostamzadeh et al. 2017; Zhao et al. 2017).

4 Conclusion

The three-dimensional flow field around airfoils with leading-edge tubercles undergoing pitch-up and hold motion has been elucidated by means of particle-tracking velocimetry (PTV) and unsteady Reynolds-averaged Navier–Stokes (RANS) simulations. This study synergistically combined measurements with an advanced 3D PTV

technique with CFD simulations for a thorough analysis of the dynamic stall process and the complex three-dimensional flow field associated with tubercled airfoils. Comparisons have been drawn between a smooth leading-edge airfoil and two airfoils equipped with tubercles in terms of the unsteady flow field and the temporal evolution of the dynamic stall vortex (DSV) and stall cells.

The tubercles cause a spatial delay in the formation of the DSV and a significant weakening of its strength. Furthermore, the tubercles modify the vortical dynamics during the growth stage of the DSV by discretizing the spanwise vorticity and concentrating it at the troughs, resulting in a DSV with reduced circulation. During pitch-up motions, the tubercles promote a stall compartmentalization mechanism. Reverse-flow regions find their inception at the tubercle troughs, leading to the formation of stall cells that become well-defined once the DSV has advected beyond the trailing edge. Finally, tubercles reduce the strength of the leading-edge vortex shedding and promote a quicker transition into the deep stall regime. At a global level, it is observed that the combination of the above factors results in a shorter and weaker lift overshoot for tubercled airfoils, thereby enhancing overall aerodynamic stability during dynamic stall conditions and promoting a quicker transition to deep stall conditions, where tubercled airfoils are known to provide higher levels of lift.

The ability of tubercles to mitigate dynamic stall has significant practical implications, especially in applications where minimizing lift hysteresis and reducing cyclic structural loads are critical. This effect could be particularly advantageous for rotorcraft, wind turbines, or other aerospace structures subject to dynamic stall, potentially enhancing operational stability and extending the lifespan of these components.

Supplementary Information The online version contains supplementary material available at <https://doi.org/10.1007/s00348-025-03981-7>.

Acknowledgements The authors acknowledge the Delft High Performance Computing Centre (DHPC) for providing computational

resources for the presented simulations. The authors would also like to extend the acknowledgement to the technical support of F. Donker Duyvis, P. Duyndam and S. Bernardy in the wind-tunnel experiment setup, as well as the assistance of O. Soare in the design and execution of the experiments.

Author contribution P.V.B. performed the experiment and simulation, collected data, prepared figures and wrote the manuscript text. S.H., F.S. and M.L. supervised the project and reviewed the manuscript.

Data availability The data supporting the findings of this study are available from the corresponding author upon reasonable request.

Declarations

Conflict of interest All authors have no conflict of interest.

Open Access This article is licensed under a Creative Commons Attribution 4.0 International License, which permits use, sharing, adaptation, distribution and reproduction in any medium or format, as long as you give appropriate credit to the original author(s) and the source, provide a link to the Creative Commons licence, and indicate if changes were made. The images or other third party material in this article are included in the article's Creative Commons licence, unless indicated otherwise in a credit line to the material. If material is not included in the article's Creative Commons licence and your intended use is not permitted by statutory regulation or exceeds the permitted use, you will need to obtain permission directly from the copyright holder. To view a copy of this licence, visit <http://creativecommons.org/licenses/by/4.0/>.

References

- Butterfield CP, Hansen AC, Simms D, Scott G (1991) Dynamic stall on wind turbine blades. In: Prepared for windpower conference and exposition, Palm Springs, California
- Borg J (2012) The Effect of Leading Edge Serrations on Dynamic Stall. Master's thesis, University of Southampton, Faculty of Engineering and the Environment, Southampton
- Buchner A-J, Soria J, Honnery D, Smits AJ (2018) Dynamic stall in vertical axis wind turbines: scaling and topological considerations. *J Fluid Mech* 841:746–766. <https://doi.org/10.1017/jfm.2018.112>
- Choudhry A, Arjomandi M, Kelso R (2013) Horizontal axis wind turbine dynamic stall predictions based on wind speed and direction variability. *Proc Inst Mech Eng Part A J Power Energy* 227:338–351. <https://doi.org/10.1177/0957650912470941>
- Caridi GAP (2018) Development and application of helium-filled soap bubbles: For large-scale PIV experiments in aerodynamics. PhD thesis, Delft University of Technology. <https://doi.org/10.4233/UUID:EFFC65F6-34DF-4EAC-8AD9-3FDB22A294DC>
- Choudhry A, Leknys R, Arjomandi M, Kelso R (2014) An insight into the dynamic stall lift characteristics. *Exp Therm Fluid Sci* 58:188–208. <https://doi.org/10.1016/j.expthermflusci.2014.07.006>
- Carr LW, Mcalister KW, McCroskey WJ (1977) Analysis of the development of dynamic stall based on oscillating airfoil experiments. Technical Report A-6674, Ames Research Center and U.S. Army Air Mobility R & D Moffett Field, Washington, D. C
- Carreira Pedro H, Kobayashi M (2008) Numerical study of stall delay on humpback whale flippers. American Institute of Aeronautics and Astronautics, Reno, Nevada. <https://doi.org/10.2514/6.2008-584>
- Custodio D (2007) The effect of humpback whale-like leading edge protuberances on hydrofoil performance. PhD thesis, Worcester Polytechnic Institute, Worcester, Massachusetts
- Cai C, Zuo ZG, Liu SH, Wu YL, Wang FB (2013) Numerical evaluations of the effect of leading-edge protuberances on the static and dynamic stall characteristics of an airfoil. *IOP Conf Ser Mater Sci Eng* 52(5):052006
- Cai C, Zuo Z, Maeda T, Kamada Y, Li Q, Shimamoto K, Liu S (2017) Periodic and aperiodic flow patterns around an airfoil with leading-edge protuberances. *Phys Fluids* 29(11):115110
- Discetti S, Agüera N, Cafiero G, Astarita T (2015) Ensemble 3D PTV for high resolution turbulent statistics (DHPC) (2024) DelftBlue Supercomputer (Phase 2). <https://www.tudelft.nl/dhpc/ark:/44463/DelftBluePhase2>
- Fish FE, Battle JM (1995) Hydrodynamic design of the humpback whale flipper. *J Morphol* 225(1):51–60
- Ferreira C, Kuik G, Bussel G, Scarano F (2009) 2D PIV visualization of dynamic stall on a vertical axis wind turbine. *Exp Fluids* 46:97–108. <https://doi.org/10.1007/s00348-008-0543-z>
- Faleiros DE, Tuinstra M, Sciacchitano A, Scarano F (2019) Generation and control of helium-filled soap bubbles for PIV. *Exp Fluids* 60(3):40
- Gendrich CP (1999) Dynamic stall of rapidly pitching airfoils. PhD thesis, Michigan State University, Department of Mechanical Engineering
- Hansen KL (2012) Effect of leading edge tubercles on airfoil performance. PhD thesis, University of Adelaide, Adelaide, South Australia
- Hryniuk JT, Bohl DG (2020) The effects of leading-edge tubercles on dynamic stall. *J Fluid Mech* 893:5
- Huang M, Ferreira C, Sciacchitano A, Scarano F (2022) Wake scaling of actuator discs in different aspect ratios. *Renew Energy* 183:866–876. <https://doi.org/10.1016/j.renene.2021.11.045>
- Jumper EJ, Schreck SJ, Dimmick RL (1987) Lift-curve characteristics for an airfoil pitching at constant rate. *J Aircr* 24(10):680–687
- Li M, Scarano F (2024) Stall cells organisation on an aerofoil with leading-edge tubercles. Submitted for publication. <https://doi.org/10.21203/rs.3.rs-4850082/v1>
- McCroskey WJ (1981) The phenomenon of dynamic stall. Technical Report A-8464, Ames Research Center, Moffett Federal Airfield, Mountain View
- Michard M, Graffieux L, Lollini L, Grosjean N (1997) Identification of vortical structures by a non-local criterion - application of PIV measurements and DNS-LES results of turbulent rotating flows. In: 11th symposium on turbulent shear flows, Grenoble, France
- Menter F, Kuntz M, Langtry R (2003) Ten years of industrial experience with the SST turbulence model. *Turbul Heat Mass Transf* 4
- Miklosovic DS, Murray MM, Howle LE (2007) Experimental evaluation of sinusoidal leading edges. *J Aircr* 44(4):1404–1408
- Nayman MN, Perez RE (2022) Improving dynamic stall effects using leading edge tubercles. In: AIAA AVIATION 2022 Forum. American Institute of Aeronautics and Astronautics, Chicago, IL & Virtual. <https://doi.org/10.2514/6.2022-3529>
- Rohmawati I, Arai H, Nakashima T, Mutsuda H, Doi Y (2020) Effect of wavy leading edge on pitching rectangular wing. *J Aero Aqua Bio-mech* 9(1):1–7
- Rostamzadeh N, Kelso RM, Dally B (2017) A numerical investigation into the effects of Reynolds number on the flow mechanism induced by a tubercled leading edge. *Theoret Comput Fluid Dyn* 31(1):1–32
- Schanz D, Gesemann S, Schröder A (2016) Shake-The-Box: Lagrangian particle tracking at high particle image densities. *Exp Fluids* 57(5):70
- Sciacchitano A, Scarano F (2014) Elimination of PIV light reflections via a temporal high pass filter. *Meas Sci Technol* 25:084009. <https://doi.org/10.1088/0957-0233/25/8/084009>
- Taylor K, Amitay M (2016). A statistical approach to the identification of vortical structures during dynamic stall with flow control.

- <https://doi.org/10.2514/6.2016-1845>.<https://api.semanticscholar.org/CorpusID:124646213>
- Visbal MR, Garmann DJ (2018) Analysis of dynamic stall on a pitching airfoil using high-fidelity large-eddy simulations. *AIAA J* 56(1):46–63
- Visbal MR (1990) Dynamic stall of a constant-rate pitching airfoil. *J Aircr* 27(5):400–407
- Wu L, Liu X (2021) Dynamic Stall Characteristics of the Bionic Airfoil with Different Waviness Ratios. *Appl Sci* 11(21):9943
- Yasuda T, Fukui K, Matsuo K, Minagawa H, Kurimoto R (2019) Effect of the Reynolds number on the performance of a NACA0012 wing with leading edge protuberance at low Reynolds numbers. *Flow Turbul Combust* 102(2):435–455
- Zhang X, Schlüter JU (2012) Numerical study of the influence of the Reynolds-number on the lift created by a leading edge vortex. *Phys Fluids* 24(6):065102
- Zhao M, Xu L, Tang Z, Zhang X, Zhao B, Liu Z, Wei Z (2021) Onset of dynamic stall of tubercled wings. *Phys Fluids* 33(8):081909
- Zhao M, Zhang M, Xu J (2017) Numerical simulation of flow characteristics behind the aerodynamic performances on an airfoil with leading edge protuberances. *Eng Appl Comput Fluid Mech* 11:193–209

Publisher's Note Springer Nature remains neutral with regard to jurisdictional claims in published maps and institutional affiliations.